

Investigation of Sub-configurations Reveals Stable Spin-Orbit Torque Switching Polarity in Polycrystalline Mn_3Sn

Boyu Zhao^{1*}, Zhengde Xu^{1*}, Xue Zhang¹, Zhenhang Kong¹, Shuyuan Shi^{2†}, and Zhifeng Zhu^{1,3‡}

¹School of Information Science and Technology, ShanghaiTech University, Shanghai, 201210,
China

²Fert Beijing Institute, MIIT Key Laboratory of Spintronics, School of Integrated Circuit Science
and Engineering, Beihang University, Beijing 100191, China

³Shanghai Engineering Research Center of Energy Efficient and Custom AI IC, Shanghai,
201210, China

Abstract

Previous studies have demonstrated the switching of octupole moment in Mn_3Sn driven by spin-orbit torque (SOT). However, they have not accounted for the polycrystalline nature of the sample when explaining the switching mechanism. In this work, we use samples with various atomic orientations to capture this polycrystalline nature. We thoroughly investigate their SOT-induced spin dynamics and demonstrate that the polycrystalline structure leads to distinct outcomes. Our findings reveal that configuration II, where the Kagome plane is perpendicular to the spin polarization, exhibits robust switching with stable polarity, whereas the signals from various sub-configurations in configuration I cancel each other out. By comparing our findings with experimental results, we pinpoint the primary sources contributing to the measured AHE signals. Additionally, we establish a dynamic balance model that incorporates the unique properties of Mn_3Sn to elucidate these observations. Our study highlights the essential role of the

polycrystalline nature in understanding SOT switching. By clarifying the underlying physical mechanisms, our work resolves the longstanding puzzle regarding the robust SOT switching observed in Mn_3Sn .

Introduction

The increasing demand for higher memory performance in modern technology has spurred extensive research into magnetic random access memory (MRAM) [1–4]. While significant advancements have been made with ferromagnetic materials [5,6], recent attention has shifted toward ferrimagnets (FiM) [7–9] or antiferromagnets (AFM) [10–17] due to their potential for faster and more energy-efficient devices. Among them, noncollinear AFM Mn_3Sn have emerged as particularly promising candidate [18–23]. The properties of Mn_3Sn are closely linked to its Kagome lattice structure [see Fig. 1(a)], which gives rise to a noncollinear spin order. As a result, despite having a negligible net magnetization, a large anomalous Hall effect (AHE) at room temperature has been demonstrated [24], which originates from the Berry curvature associated with its topological band structure. These unique properties in Mn_3Sn open avenues for promising spintronic applications [25,26], such as racetrack memory [27–29] and unconventional computing [30–36].

For the electrical manipulation of magnetic states in Mn_3Sn , it has been experimentally demonstrated that spin–orbit torque (SOT) can be used to switch the polycrystalline samples [37]. To understand the underlying switching mechanisms, the samples are classified into three different configurations based on the relative alignment between the Kagome plane, the spin polarization

(σ), and the external magnetic field (\mathbf{H}_{ext}) [see Fig. 1(b)]. By excluding configuration III, which does not contribute to the perpendicular magnetization, it was concluded that configuration I exhibits switching behavior, whereas there is only oscillation in configuration II [37–39]. However, the switching mechanism in configuration I is still under debate [40], and subsequent works [41–43] have also identified deterministic switching in configuration II. In particular, our previous work [43] demonstrates that a strain-induced change in anisotropy is not necessarily required to achieve deterministic switching. We also show that the switching results in configuration II is insensitive to the initial state, making it more suitable for memory applications.

Although the spin dynamics of both configurations I and II have been extensively studied [43,44]. It should be aware that using only these three different configurations is insufficient to capture the polycrystalline nature of the sample [see Fig. 1(c)]. In fact, any orientation of the Kagome plane is possible, e.g., rotating the sample within the Kagome plane by 90° creates a distinct atomic environment for the spin states. To address this, we propose rotating the samples of configurations I and II through all angles in the range $\varphi = [0^\circ, 360^\circ]$ to capture all possible atomic states [see Fig. 2(b)]. By measuring the AHE signals, experimental studies have demonstrated robust SOT-induced switching in polycrystalline samples [7,9,17]. However, the contributions of different sub-configurations to the measured AHE signals remain unclear. In this work, by employing a more detailed methodology to examine the atomic states in polycrystalline samples, we conclude that the SOT-induced switching in configuration I will be balanced out, whereas configuration II contributes significantly to the measured AHE signals. Additionally, we propose a dynamic balance model that fully explains our results.

Methodology

The device studied in this work consists of Mn₃Sn and Pt bilayer [see Fig. 1(c)]. A charge current flowing through the heavy metal layer produces SOT [46–49] that affects the spin dynamics of Mn₃Sn. The Hamiltonian describing the system is expressed as:

$$\mathcal{H} = \sum_{i \neq j} A_{ij} \mathbf{m}_i \cdot \mathbf{m}_j + \sum_{i \neq j} \mathbf{D}_{ij} \cdot (\mathbf{m}_i \times \mathbf{m}_j) - \sum_i (\mathbf{K}_i \cdot \mathbf{m}_i)^2 - \mu_0 \mu_i \sum_i (\mathbf{m}_i \cdot \mathbf{H}_{\text{ext}}),$$

where the exchange constant $A = 17.53$ meV, the Dzyaloshinskii-Moriya interaction (DMI) [50,51] constant $D = 0.833$ meV, the magnetic anisotropy constant $K = 0.196$ meV [18], and the magnetic moment $\mu = 3\mu_B$. The magnetic dynamics is obtained by solving the coupled Landau-Lifshitz-Gilbert-Slonczewski (LLGS) equations for the three Mn atoms in the same layer [52,53]:

$$\frac{d\mathbf{m}_i}{dt} = -\gamma \mathbf{m}_i \times \mathbf{H}_{\text{eff},i} + \alpha \mathbf{m}_i \times \frac{d\mathbf{m}_i}{dt} - \gamma \theta_{\text{SH}} \frac{J_c}{2eM_s d} \mathbf{m}_i \times (\mathbf{m}_i \times \sigma_i).$$

The three terms on the right-hand side represent the precession, Gilbert damping, and damping-like SOT, respectively. Here, γ is the gyromagnetic ratio, $\alpha = 0.003$ [37] is the Gilbert damping constant, and the spin Hall angle θ_{SH} is 0.06 [41]. The effective field $\mathbf{H}_{\text{eff},i}$ is derived from the Hamiltonian as $\mathbf{H}_{\text{eff},i} = -\frac{1}{\mu_i} \frac{\partial \mathcal{H}}{\partial \mathbf{m}_i}$, and the thickness of Mn₃Sn film $d = 30$ nm [41], the saturation magnetization $M_s = 6\mu/V_{\text{cell}}$ [37] with the unit cell volume $V_{\text{cell}} = 0.3778$ nm³. The LLGS equations are solved using the fourth-order Runge-Kutta method with a time step of 5 fs.

Results and Discussion

As illustrated in Fig. 2(a), we rotate the Kagome plane counterclockwise by an increment

angle of 1° to create 360 distinct sub-configurations denoted as $\varphi_{\text{sub_conf}}$. Noted that the sub-configurations constructed in this procedure cover all the possible orientations that exist in the polycrystalline sample. For each sub-configuration, we then apply the same \mathbf{J}_c and \mathbf{H}_{ext} and observe its SOT-driven dynamics. The results are shown in Fig. 2(b), where the final state denoted by φ_{Final} reveals six periods. Within each period, φ_{Final} linearly increases with the rotation angle, indicating the alignment of octupole magnetic moment with the same easy axis within the Kagome plane. Towards the end of each period, a notable transition of φ_{Final} occurs, meaning that the octupole moment is shifted to another easy axis. It is important to notice that φ_{Final} of all the sub-configurations is restricted within -14° to 46° [marked by the blue region in the inset of Fig. 2(b)], all of which have $m_{z,\text{oct}} > 0$. Reversing the current leads to an opposite switching to $m_{z,\text{oct}} < 0$. This indicates that for configuration II, successful magnetization switching is achieved in all sample orientations, significantly contributing to the experimentally measured AHE signals. In other words, the SOT-driven switching of configuration II exhibits a stable polarity.

To further understand the switching process, we then investigate their magnetization dynamics by choosing some representative sub-configurations marked by the green and red dots. The three green dots correspond to the rotation of crystallize lattice $\varphi_{\text{sub-conf}} = 55^\circ, 175^\circ, \text{ and } 295^\circ$, as sketched in the left inset of Fig. 2(c). Noted that they have an identical atomic environment, i.e., the triangle consisted of the three red atoms points in the same direction. When $\mathbf{J}_c = 5 \times 10^{10} \text{ A/m}^2$ and $\mathbf{H}_{\text{ext}} = 100 \text{ Oe}$ are applied along the $+\mathbf{y}$ axis, deterministic switching is achieved, and all the three sub-configurations are switched to the same final state with $\varphi_{\text{Final}} = -5^\circ$ as shown in the right inset of Fig. 2(c). This reproduces our previous results [43] that the initial states with the same atomic

environment will be switched to the same final state under suitable \mathbf{J}_c and \mathbf{H}_{ext} . Different from the green dots that represent the early phase of a period, we then choose three sub-configurations marked by red dots that represent the late phase. As shown in the left inset of Fig. 2(d), they have the same atomic environments but different spin configuration with $\varphi_{\text{sub-conf}} = 30^\circ, 150^\circ, \text{ and } 270^\circ$. Under the same \mathbf{J}_c and \mathbf{H}_{ext} , all of them are switched to the same final state with $\varphi_{\text{Final}} = 30^\circ$. Comparing the switching results in Figs. 2(c) and 2(d), we can more intuitively understand the periodicity observed in Fig. 2(b). As the sample is rotated (cf. $\varphi_{\text{sub-conf}}$), the final state φ_{Final} also rotates in the same direction, exhibiting a periodicity of 60° from -14° to 46° .

Recall that in our previous work [43], we find that the switching result is independent of the initial state. One might conclude that the results observed here can also be explained using our previous analysis. For example, under a fixed \mathbf{J}_c and \mathbf{H}_{ext} , the octupole moment is switched to a fixed angle with $\varphi = 16^\circ$. After removing \mathbf{J}_c and \mathbf{H}_{ext} , the octupole moment is relaxed to the nearest easy axis. Since the easy axis rotates with the sample, it will provide a switching diagram exact the same as Fig. 2(b). However, by looking at Fig. 3(a), where φ_{Mid} is defined as the state of octupole moment when both \mathbf{J}_c and \mathbf{H}_{ext} remain turns on, one can immediately realize that the results presented here cannot be explained using the abovementioned analysis. In contrast to the assumption that the octupole moment is fixed at $\varphi = 16^\circ$, we find that φ_{Mid} also rotates, and it again reveals six periods. In addition, the φ_{Mid} covers the region marked by pink, which has different ranges from φ_{Final} that is marked by blue. We want to emphasize that the conclusion from our previous work remains valid, i.e., for the sub-configurations with the same atomic environment, φ_{Final} is the same regardless of the spin configuration. The switching results of the three sub-

configurations in our previous work are marked by the red dots in Fig. 3(a). It is evident that our previous study represents a subset of the complete results presented here.

In our previous work, we show that stable switching of Mn₃Sn is achieved by the balance of SOT effective field $\mathbf{H}_{\text{DL}} = \boldsymbol{\sigma} \times \mathbf{m}_{\text{oct}}$ and \mathbf{H}_{ext} , where the handedness anomaly in the Mn₃Sn system is also included [42]. However, since \mathbf{H}_{ext} is fixed while \mathbf{H}_{DL} varies with φ_{Mid} , the balance of only two effective fields cannot justify the variation of φ_{Final} and φ_{Mid} as observed in Fig. 2(b) and Fig. 3(a). In addition, it is also important to explain why the octupole moments are restricted within a specific range. As both φ_{Final} and φ_{Mid} exhibit six periods, this motivates us to propose a theoretical model that includes the anisotropy energy, which also has six-fold easy axis. The anisotropy field of Mn₃Sn can be expressed as $\mathbf{H}_{\text{an}} = (\mathbf{m}_{\text{oct}} \cdot \mathbf{e})\mathbf{e} - \mathbf{m}_{\text{oct}}$, where \mathbf{e} denotes the direction of the easy axis. As shown in Fig. 3(b), \mathbf{H}_{an} points from the octupole moment and perpendicular to the easy axis. The \mathbf{H}_{ext} and \mathbf{H}_{DL} determine the approximate direction of the octupole moment, and the easy axis near this direction provides an appropriate \mathbf{H}_{an} . The equilibrium state of Mn₃Sn results from the vector balance among these three fields, which is sketched in Fig. 3(b). This is further supported by the relationship between $\varphi_{\text{sub-conf}}$ and φ_{Diff} , where φ_{Diff} is defined as $|\varphi_{\text{Final}} - \varphi_{\text{Mid}}|$. As shown in Fig. 3(c), φ_{Diff} shows a trend of being highest at both ends of the period and lowest in the middle. Since the anisotropy energy $E_{\text{an}} = -K_{\text{u}}(\mathbf{e} \cdot \mathbf{m}_{\text{oct}})^2$ [54], \mathbf{m}_{oct} tends to align more closely with the easy axis direction to minimize E_{an} . As the system approaches stability, the resulting \mathbf{H}_{an} will also decrease in magnitude. Therefore, we have established a dynamic theoretical model to explain the observed results. As shown in Fig. 3(d), we assume that the Mn₃Sn system is initially stabilized under the balance of \mathbf{H}_{ext} , $\mathbf{H}_{\text{DL},1}$ and $\mathbf{H}_{\text{an},1}$

(point A). The system is then rotated to point B, accompanied by the rotation of Kagome plane. It is important to note that while the direction and magnitude of \mathbf{H}_{ext} is fixed, \mathbf{H}_{DL} has a fixed magnitude but a varied direction that depends on \mathbf{m}_{oct} , and \mathbf{H}_{an} is always perpendicular to the easy axis. The stability of the system now requires the balance between \mathbf{H}_{ext} , $\mathbf{H}_{\text{DL},2}$ and $\mathbf{H}_{\text{an},2}$. Therefore, during the rotation of the sample from point A to point B as indicated by the black arrow, \mathbf{H}_{DL} and \mathbf{H}_{an} are adjusted accordingly to maintain the balance. The magnitude of \mathbf{H}_{an} will reach its minimum value at a specific position. Within a 60° range around this position [indicated by the orange region in Fig. 3(d)], the required \mathbf{H}_{an} to maintain the balance of the three vectors is relatively small. However, if the system is rotated out of this region, the \mathbf{H}_{an} (the dashed red arrow) that required to balance the \mathbf{H}_{DL} (the cyan dashed arrow) becomes overwhelmingly larger. This state denoted by the dashed arrows is thus unstable. Since the six easy axes of Mn_3Sn are evenly distributed, one of the easy axes will always appear in the comfort region marked by orange. Once the system is rotated beyond this region, it will be realigned back to minimize the system energy. The dynamic balance model proposed here perfectly explains the variation of φ_{Diff} , which reflects \mathbf{H}_{an} , and the appearance of six periods shown in Fig. 3(c). As a result, all the sub-configurations of configuration II will be switched to the easy axis within a specific region, leading to a stable switching polarity.

Similarly, the SOT induced spin dynamics in configuration I is examined by constructing the sub-configurations as shown in Fig. 4(a). Fig. 4(b) shows the relationship between φ_{Final} and all the 360 sub-configurations under $\mathbf{J}_c = 2.2 \times 10^{14} \text{ A/m}^2$ and $\mathbf{H}_{\text{ext}} = 1000 \text{ Oe}$, which is the suitable switching condition revealed in our previous work [43]. It shows that switching does not occur for

the $\varphi_{\text{sub-conf}}$ within $[0^\circ, 59^\circ]$, $[120^\circ, 240^\circ]$ and $[301^\circ, 360^\circ]$. Fig. 4(c) shows the octupole dynamics of two $\varphi_{\text{sub-conf}}$ from these intervals, i.e., $\varphi_{\text{sub-conf}} = 160^\circ$ and $\varphi_{\text{sub-conf}} = 340^\circ$, where one can clearly see that the magnetic states remain unchanged. In contrast, SOT-induced switching occurs within four intervals, i.e., $[60^\circ, 90^\circ]$, $[91^\circ, 119^\circ]$, $[241^\circ, 269^\circ]$, and $[270^\circ, 300^\circ]$. The octupole dynamics of two exemplary $\varphi_{\text{sub-conf}}$, i.e., $\varphi_{\text{sub-conf}} = 75^\circ$ and $\varphi_{\text{sub-conf}} = 105^\circ$, is shown in Fig. 4(d). It is intriguing to see that under the same \mathbf{J}_c and \mathbf{H}_{ext} , \mathbf{m}_{oct} is switched from $+\mathbf{z}$ direction to a $-\mathbf{z}$ for $\varphi_{\text{sub-conf}} = 75^\circ$, whereas an opposite switching is observed for $\varphi_{\text{sub-conf}} = 105^\circ$.

The switching results of configurations II and I are summarized into the polarity diagrams as shown in Fig. 5. In configuration II, the magnetic octupole of any sub-configuration is switched to the $[-14^\circ, 46^\circ]$ interval, as indicated by the dark-colored region. Noted that all of them are directed towards the $+\mathbf{z}$ direction. In configuration I, the previously mentioned four switching intervals are marked by the light-colored regions in Fig. 5(b). Regions g and b with $+\mathbf{z}$ components are switched to regions e and d that point to $-\mathbf{z}$ direction, whereas regions f and c are switched from $-\mathbf{z}$ to $+\mathbf{z}$ direction. These comparable and opposite switching polarities in configuration I will be compensated, and the overall switching will not exhibit a preferred direction when these sub-configurations are evenly distributed. As a result, the spin reorientation in configuration I has a minimal contribution to the AHE signals measured in experiments.

Based on these results, now we can discuss the previous experimental findings. Ref. [17] studied SOT switching of Mn_3Sn by rotating the Hall bar device, which is similar to the procedure of constructing sub-configurations conducted in our study. They have reported deterministic switching across all rotation angles. Our results show that the measured AHE signals should be

primarily contributed by configuration II, whereas the signals from configuration I are weak due to their compensating characteristics.

Conclusion

By examining the different atomic orientations present in the polycrystalline Mn_3Sn sample, we find that the sub-configurations in configuration II consistently contribute to a positive m_z component, which is switched to the opposite state when either \mathbf{J}_c or \mathbf{H}_{ext} is reversed. In contrast, the signals are cancelled out in configuration I. This demonstrates that configuration II exhibits a stable polarity of SOT-driven switching, resulting in measurable AHE signals in experiments. In addition, the switching behavior reveals periodic repetition with a period of 60° . Based on this, we propose a dynamic balance model that incorporates the six-fold anisotropy present in Mn_3Sn . By comparing our results with experimental data, this work provides a comprehensive understanding of the switching mechanism in polycrystalline Mn_3Sn . Additionally, we provide guidelines for the design of efficient Mn_3Sn -based MRAM devices.

*Boyu Zhao and Zhengde Xu contributed equally to this work.

†Corresponding Author: smeshis@buaa.edu.cn

‡Corresponding Author: zzfmvp@gmail.com

The data that support the findings of this study are available from the corresponding author upon reasonable request.

Acknowledgments: This work was supported by National Key R&D Program of China (Grant No. 2024YFB3614100). The simulation conducted in this work is supported by HPC Platform and SIST Computing Platform at ShanghaiTech University.

Figures

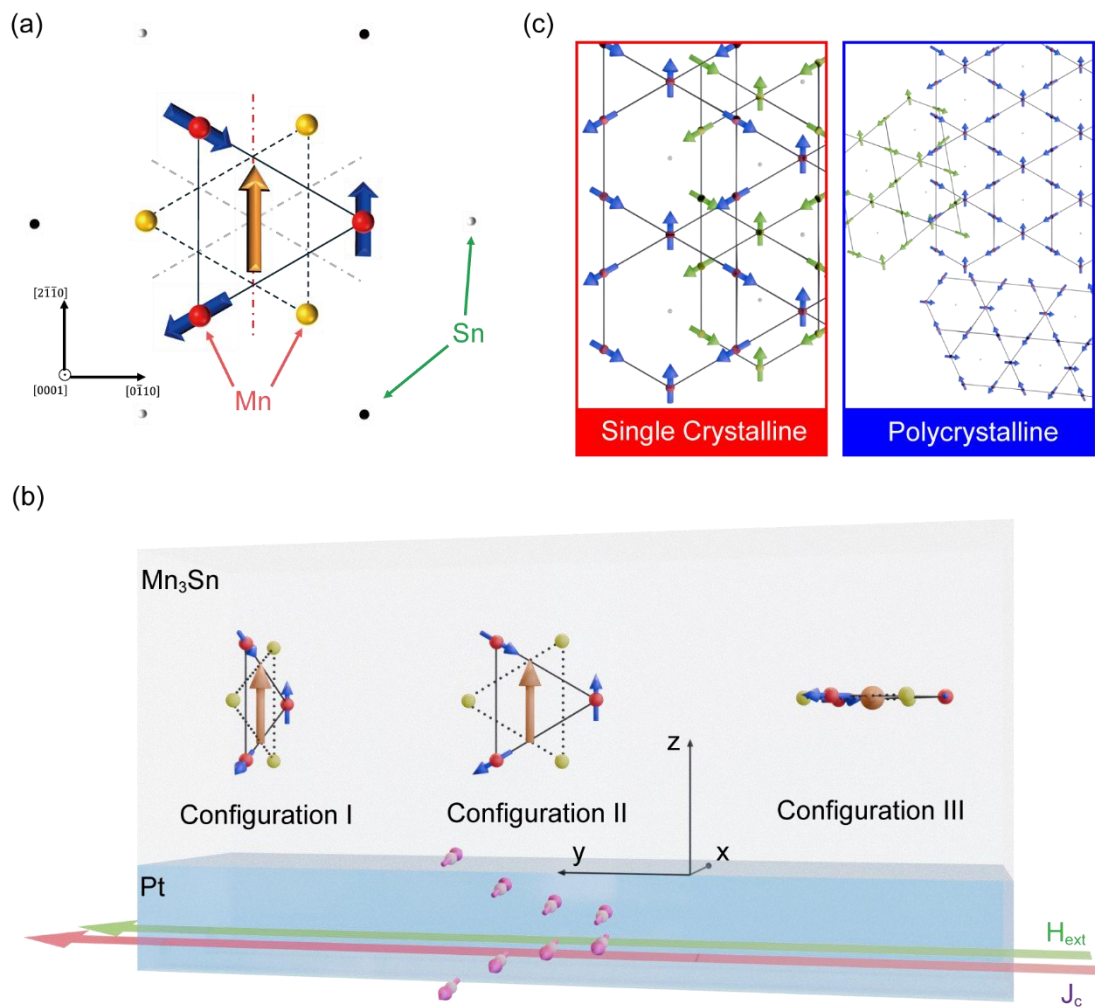


FIG. 1. (a) Atomic structure of Mn_3Sn . The red and yellow circles denote Mn atoms on the different layers. The black and silver circles denote Sn atoms on the same layer of red and yellow Mn,

respectively. Red and gray dashed lines represent easy axes of magnetic octupole. (b) The three device configurations. The Kagome plane is perpendicular to \mathbf{H}_{ext} and parallel to $\boldsymbol{\sigma}$ in configuration I. The Kagome plane is parallel to \mathbf{H}_{ext} and perpendicular to $\boldsymbol{\sigma}$ in configuration II. The Kagome plane is parallel to both \mathbf{H}_{ext} and $\boldsymbol{\sigma}$ in configuration III. (c) Schematic illustration of the single crystalline and polycrystalline structures.

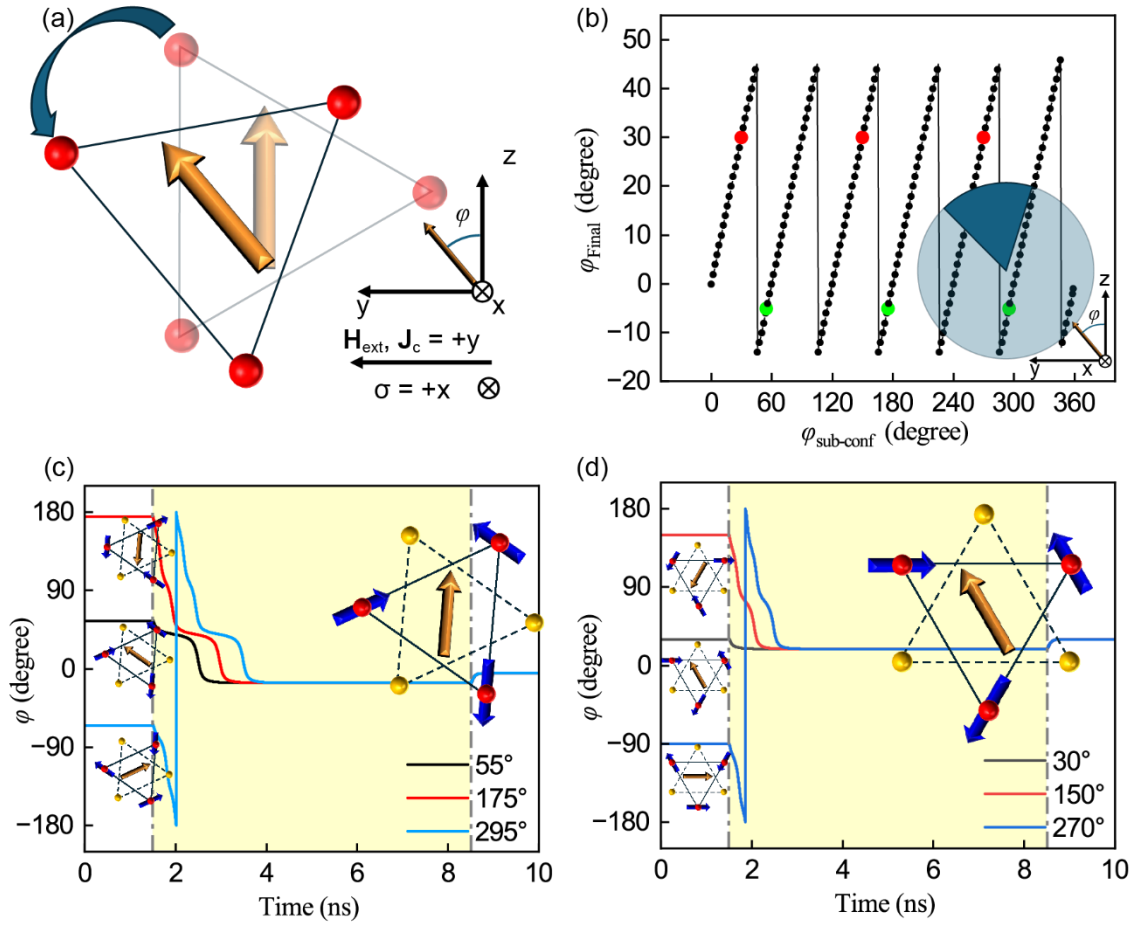


FIG. 2. (a) Starting from the $+z$ direction with $\varphi_{\text{sub-conf}} = 0$, sub-configurations of configuration II are constructed by rotating the sample counterclockwise with 1° increments. At the same time, the dynamics of octupole moment is investigated under $\mathbf{J}_c = 5 \times 10^{10}$ A/m² and $\mathbf{H}_{\text{ext}} = 100$ Oe that are applied along the $+y$ axis. (b) Relationship between φ_{Final} and $\varphi_{\text{sub-conf}}$. The dark blue region in the inset indicates the range of the final state. Dynamics of octupole moment starting from (c) $\varphi = 30^\circ, 150^\circ, 270^\circ$ and (d) $\varphi = 55^\circ, 175^\circ, 295^\circ$, respectively.

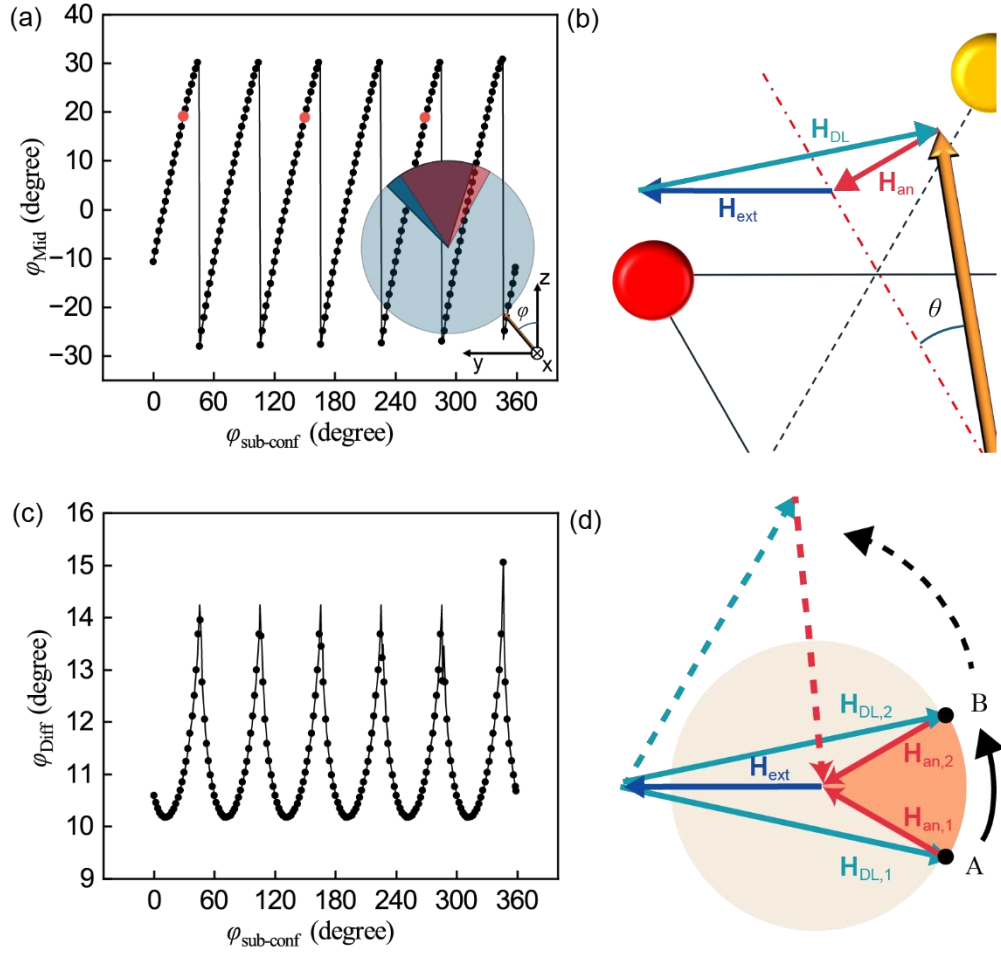


FIG. 3. (a) Relationship between φ_{Mid} and $\varphi_{\text{sub-conf}}$. The red region in the inset indicates the range of the middle state. (b) An equilibrium state of the magnetic octupole under \mathbf{H}_{DL} , \mathbf{H}_{ext} , and \mathbf{H}_{an} . The red dashed line denotes the dominant easy axis. (c) Relationship between angle difference φ_{Diff} and $\varphi_{\text{sub-conf}}$. (d) Dynamic balance model that integrates the three effective fields and the rotation of the sample. Note that the diagram (d) describes the effective fields, the corresponding octupole moment is denoted by the dark blue region shown in (a).

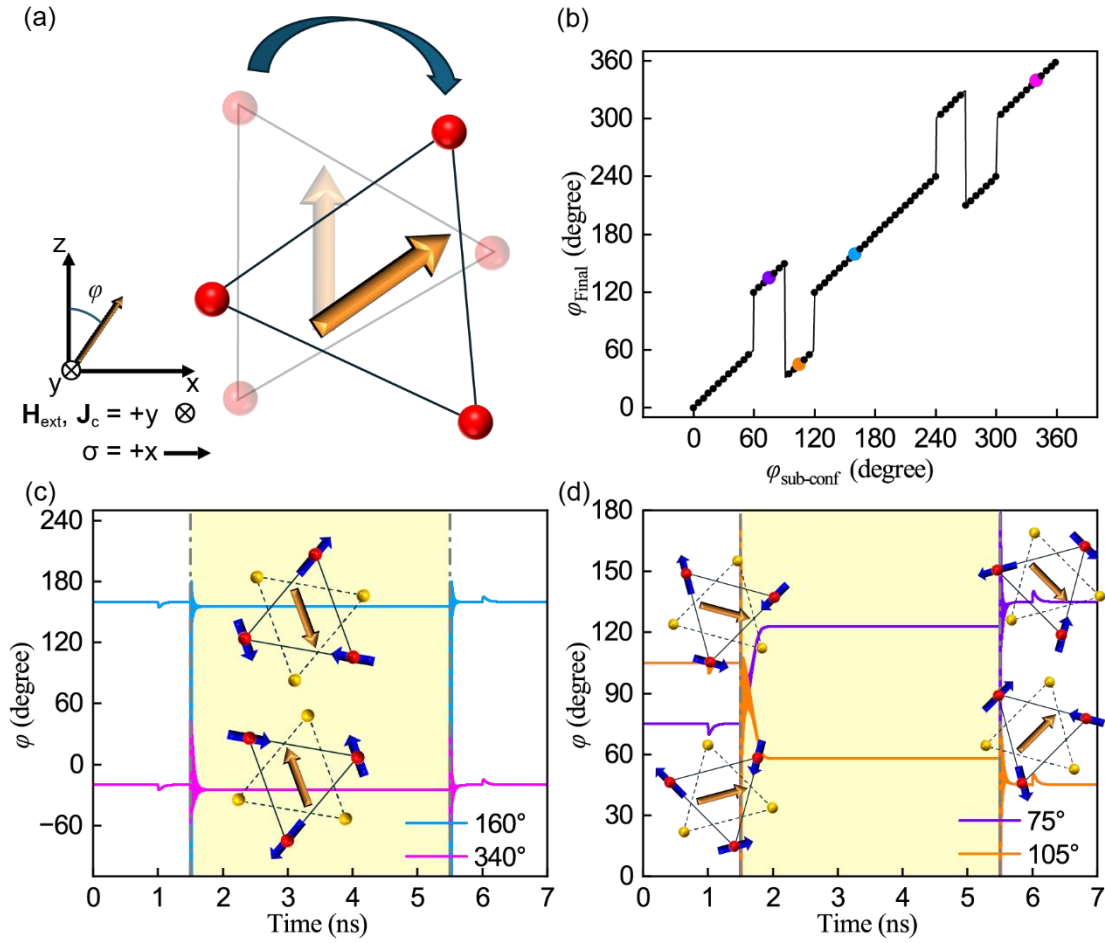


FIG. 4. (a) Construction of sub-configurations in configuration I. (b) Relationship between φ_{Final} and $\varphi_{\text{sub-conf}}$. Dynamics of octupole moment starting from (c) $\varphi = 160^\circ, 340^\circ$ and (d) $\varphi = 75^\circ, 105^\circ$, respectively.

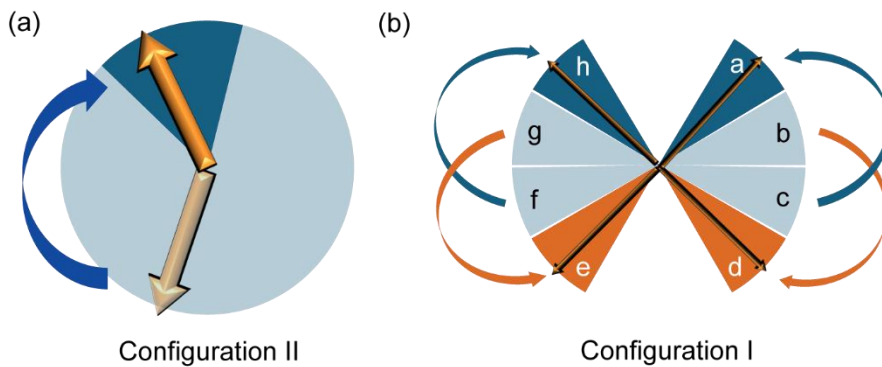


FIG. 5. Polarity diagrams of configurations (a) II and (b) I. The arrows denote the switching

direction of octupole moment.

References

- [1] X. Zhang, Z. Xu, and Z. Zhu, Revisiting the analytical solution of spin-orbit torque switched nanoscale perpendicular ferromagnets, *Phys. Rev. B* **110**, 184428 (2024).
- [2] J.-G. Zhu and A. Shadman, Resonant Spin-Transfer Torque Magnetoresistive Memory, *IEEE Trans. Magn.* **55**, 1 (2019).
- [3] D. Zhang et al., Bipolar Electric-Field Switching of Perpendicular Magnetic Tunnel Junctions through Voltage-Controlled Exchange Coupling, *Nano Lett.* **22**, 622 (2022).
- [4] A. K. Biswas, H. Ahmad, J. Atulasimha, and S. Bandyopadhyay, Experimental Demonstration of Complete 180° Reversal of Magnetization in Isolated Co Nanomagnets on a PMN–PT Substrate with Voltage Generated Strain, *Nano Lett.* **17**, 3478 (2017).
- [5] L. Liu, O. J. Lee, T. J. Gudmundsen, D. C. Ralph, and R. A. Buhrman, Current-Induced Switching of Perpendicularly Magnetized Magnetic Layers Using Spin Torque from the Spin Hall Effect, *Phys. Rev. Lett.* **109**, 096602 (2012).
- [6] C.-F. Pai, L. Liu, Y. Li, H. W. Tseng, D. C. Ralph, and R. A. Buhrman, Spin transfer torque devices utilizing the giant spin Hall effect of tungsten, *Appl. Phys. Lett.* **101**, 122404 (2012).
- [7] M. Lonsky and A. Hoffmann, Coupled skyrmion breathing modes in synthetic ferri- and antiferromagnets, *Phys. Rev. B* **102**, 104403 (2020).
- [8] M. G. Morshed, K. H. Khoo, Y. Quessab, J.-W. Xu, R. Laskowski, P. V. Balachandran, A. D. Kent, and A. W. Ghosh, Tuning Dzyaloshinskii-Moriya interaction in ferrimagnetic GdCo: A first-principles approach, *Phys. Rev. B* **103**, 174414 (2021).
- [9] N. Roschewsky, C.-H. Lambert, and S. Salahuddin, Spin-orbit torque switching of ultralarge-thickness ferrimagnetic GdFeCo, *Phys. Rev. B* **96**, 064406 (2017).
- [10] Z. Xu, J. Ren, Z. Yuan, Y. Xin, X. Zhang, S. Shi, Y. Yang, and Z. Zhu, Field-free spin-orbit torque switching of an antiferromagnet with perpendicular Néel vector, *J. Appl. Phys.* **133**, 153904 (2023).
- [11] Y. Qiao, Z. Xu, Z. Xu, Y. Yang, and Z. Zhu, Orthogonal spin-orbit torque-induced deterministic switching in NiO, *Appl. Phys. Lett.* **125**, 182403 (2024).
- [12] E. A. Tremsina and G. S. D. Beach, Atomistic simulations of distortion-limited high-speed dynamics of antiferromagnetic skyrmions, *Phys. Rev. B* **106**, L220402 (2022).
- [13] C. Schmitt et al., Identification of Néel Vector Orientation in Antiferromagnetic Domains Switched by Currents in Ni O / Pt Thin Films, *Phys. Rev. Appl.* **15**, 034047 (2021).
- [14] Y. M. Hung, Y. Shiota, S. Yamada, M. Ohta, T. Shibata, T. Sasaki, R. Hisatomi, T. Moriyama, and T. Ono, Positive correlation between interlayer exchange coupling and the driving current of domain wall motion in a synthetic antiferromagnet, *Appl. Phys. Lett.* **119**, 032407 (2021).
- [15] D.-F. Shao and E. Y. Tsybal, Antiferromagnetic tunnel junctions for spintronics, *Npj Spintron.* **2**, 13 (2024).
- [16] X. Chen et al., Control of spin current and antiferromagnetic moments via topological surface state, *Nat. Electron.* **5**, 574 (2022).
- [17] J. Lu et al., Voltage-gated spin-orbit torque switching in IrMn-based perpendicular magnetic tunnel junctions, *Appl. Phys. Lett.* **122**, 012402 (2023).

- [18] T. Nagamiya, S. Tomiyoshi, and Y. Yamaguchi, Triangular spin configuration and weak ferromagnetism of Mn_3Sn and Mn_3Ge , *Solid State Commun.* **42**, 385 (1982).
- [19] T. F. Duan, W. J. Ren, W. L. Liu, S. J. Li, W. Liu, and Z. D. Zhang, Magnetic anisotropy of single-crystalline Mn_3Sn in triangular and helix-phase states, *Appl. Phys. Lett.* **107**, 082403 (2015).
- [20] Y. Deng, X. Liu, Y. Chen, Z. Du, N. Jiang, C. Shen, E. Zhang, H. Zheng, H.-Z. Lu, and K. Wang, All-electrical switching of a topological non-collinear antiferromagnet at room temperature, *Natl. Sci. Rev.* **10**, nwac154 (2023).
- [21] J. Shi et al., Electrically Controlled All-Antiferromagnetic Tunnel Junctions on Silicon with Large Room-Temperature Magnetoresistance, *Adv. Mater.* **36**, 2312008 (2024).
- [22] H. Xie, X. Chen, Q. Zhang, Z. Mu, X. Zhang, B. Yan, and Y. Wu, Magnetization switching in polycrystalline Mn_3Sn thin film induced by self-generated spin-polarized current, *Nat. Commun.* **13**, 5744 (2022).
- [23] D. P. Goli and S. K. Kim, *Terahertz Magnon Excitations and Switching in Non-Collinear Antiferromagnets*, arXiv:2501.01150.
- [24] S. Nakatsuji, N. Kiyohara, and T. Higo, Large anomalous Hall effect in a non-collinear antiferromagnet at room temperature, *Nature* **527**, 212 (2015).
- [25] S. Hu, C. Zheng, W. Fan, and Y. Liu, Terahertz magnetic excitations in non-collinear antiferromagnetic Mn_3Pt : Atomistic-scale dynamical simulations, *J. Magn. Magn. Mater.* **588**, 171393 (2023).
- [26] A. Haldar and A. O. Adeyeye, Microwave assisted gating of spin wave propagation, *Appl. Phys. Lett.* **116**, 162403 (2020).
- [27] K.-J. Kim et al., Fast domain wall motion in the vicinity of the angular momentum compensation temperature of ferrimagnets, *Nat. Mater.* **16**, 1187 (2017).
- [28] M. Wu et al., Current-driven fast magnetic octupole domain-wall motion in noncollinear antiferromagnets, *Nat. Commun.* **15**, 4305 (2024).
- [29] H. Isshiki, N. Budai, A. Kobayashi, R. Uesugi, T. Higo, S. Nakatsuji, and Y. Otani, Observation of Cluster Magnetic Octupole Domains in the Antiferromagnetic Weyl Semimetal Mn_3Sn Nanowire, *Phys. Rev. Lett.* **132**, 216702 (2024).
- [30] M. Romera et al., Vowel recognition with four coupled spin-torque nano-oscillators, *Nature* **563**, 230 (2018).
- [31] K. Y. Camsari, R. Faria, B. M. Sutton, and S. Datta, Stochastic p -Bits for Invertible Logic, *Phys. Rev. X* **7**, 031014 (2017).
- [32] C. Niu et al., A self-learning magnetic Hopfield neural network with intrinsic gradient descent adaption, *Proc. Natl. Acad. Sci.* **121**, e2416294121 (2024).
- [33] S. Luo, N. Xu, Z. Guo, Y. Zhang, J. Hong, and L. You, Voltage-Controlled Skyrmion Memristor for Energy-Efficient Synapse Applications, *IEEE Electron Device Lett.* **40**, 635 (2019).
- [34] X. Li et al., Restricted Boltzmann Machines Implemented by Spin–Orbit Torque Magnetic Tunnel Junctions, *Nano Lett.* **24**, 5420 (2024).
- [35] G. K. Krishnaswamy, G. Sala, B. Jacot, C.-H. Lambert, R. Schlitz, M. D. Rossell, P. Noël, and P. Gambardella, Time-Dependent Multistate Switching of Topological Antiferromagnetic Order in Mn_3Sn , *Phys. Rev. Appl.* **18**, 024064 (2022).
- [36] Z. Zheng et al., Effective electrical manipulation of a topological antiferromagnet by orbital torques, *Nat. Commun.* **15**, 745 (2024).
- [37] H. Tsai et al., Electrical manipulation of a topological antiferromagnetic state, *Nature* **580**, 608 (2020).

- [38] D.-Y. Zhao, P.-B. He, and M.-Q. Cai, Terahertz oscillation in a noncollinear antiferromagnet under spin-orbit torques, *Phys. Rev. B* **104**, 214423 (2021).
- [39] A. Shukla and S. Rakheja, Spin-Torque-Driven Terahertz Auto-Oscillations in Noncollinear Coplanar Antiferromagnets, *Phys. Rev. Appl.* **17**, 034037 (2022).
- [40] B. Pal et al., Setting of the magnetic structure of chiral kagome antiferromagnets by a seeded spin-orbit torque, *Sci. Adv.* **8**, eabo5930 (2022).
- [41] T. Higo et al., Perpendicular full switching of chiral antiferromagnetic order by current, *Nature* **607**, 474 (2022).
- [42] J.-Y. Yoon et al., Handedness anomaly in a non-collinear antiferromagnet under spin-orbit torque, *Nat. Mater.* **22**, 1106 (2023).
- [43] Z. Xu, X. Zhang, Y. Qiao, G. Liang, S. Shi, and Z. Zhu, Deterministic spin-orbit torque switching including the interplay between spin polarization and kagome plane in Mn_3Sn , *Phys. Rev. B* **109**, 134433 (2024).
- [44] A. Shukla, S. Qian, and S. Rakheja, Impact of strain on the SOT-driven dynamics of thin film Mn_3Sn , *J. Appl. Phys.* **135**, 123903 (2024).
- [45] T. Xu, H. Bai, Y. Dong, L. Zhao, H.-A. Zhou, J. Zhang, X.-X. Zhang, and W. Jiang, Robust spin torque switching of noncollinear antiferromagnet Mn_3Sn , *APL Mater.* **11**, 071116 (2023).
- [46] D. Polley, A. Pattabi, A. Rastogi, K. Jhuria, E. Diaz, H. Singh, A. Lemaitre, M. Hehn, J. Gorchon, and J. Bokor, Picosecond spin-orbit torque-induced coherent magnetization switching in a ferromagnet, *Sci. Adv.* **9**, eadh5562 (2023).
- [47] Y. Zhang et al., Room temperature field-free switching of perpendicular magnetization through spin-orbit torque originating from low-symmetry type II Weyl semimetal, *Sci. Adv.* **9**, eadg9819 (2023).
- [48] Y. Guo et al., Controllable conical magnetic structure and spin-orbit-torque switching in symmetry-broken ferrimagnetic films, *Phys. Rev. Appl.* **21**, 014045 (2024).
- [49] L. Zhu and D. C. Ralph, Strong variation of spin-orbit torques with relative spin relaxation rates in ferrimagnets, *Nat. Commun.* **14**, 1778 (2023).
- [50] F. Liu, T. Huang, L. Hai, Z. Shi, X. Qiu, S. M. Zhou, and W. Fan, Effects of asymmetric Dzyaloshinskii-Moriya interaction on non-collinear antiferromagnetic spin chiral switching, *SPIN* (2024).
- [51] S. D. Pollard, J. A. Garlow, K.-W. Kim, S. Cheng, K. Cai, Y. Zhu, and H. Yang, Bloch Chirality Induced by an Interlayer Dzyaloshinskii-Moriya Interaction in Ferromagnetic Multilayers, *Phys. Rev. Lett.* **125**, 227203 (2020).
- [52] X. Zhang, B. Cai, J. Ren, Z. Yuan, Z. Xu, Y. Yang, G. Liang, and Z. Zhu, Spatially nonuniform oscillations in ferrimagnets based on an atomistic model, *Phys. Rev. B* **106**, 184419 (2022).
- [53] R. F. L. Evans, W. J. Fan, P. Chureemart, T. A. Ostler, M. O. A. Ellis, and R. W. Chantrell, Atomistic spin model simulations of magnetic nanomaterials, *J. Phys. Condens. Matter* **26**, 103202 (2014).
- [54] E. C. Stoner and E. P. Wohlfarth, A mechanism of magnetic hysteresis in heterogeneous alloys, *IEEE Trans. Magn.* **27**, 3475 (1991).